Highly dynamic gamma-ray emissions are common in tropical thunderclouds

https://doi.org/10.1038/s41586-024-07936-6

Received: 4 February 2024

Accepted: 7 August 2024

Published online: 2 October 2024



Check for updates

M. Marisaldi^{1,2,∞}, N. Østgaard^{1,∞}, A. Mezentsev^{1,∞}, T. Lang³, J. E. Grove⁴, D. Shy⁴,

G. M. Heymsfield⁵, P. Krehbiel⁶, R. J. Thomas⁶, M. Stanley⁶, D. Sarria¹, C. Schultz³,

R. Blakeslee³, M. G. Quick³, H. Christian⁷, I. Adams⁵, R. Kroodsma⁵, N. Lehtinen¹, K. Ullaland¹,

S. Yang¹, B. Hasan Qureshi¹, J. Søndergaard¹, B. Husa¹, D. Walker⁷, M. Bateman⁷, D. Mach⁸,

S. Cummer⁹, M. Pazos¹⁰, Y. Pu⁹, P. Bitzer⁷, M. Fullekrug¹¹, M. Cohen¹², J. Montanya¹³,

C. Younes¹⁴, O. van der Velde¹³, J. A. Roncancio¹³, J. A. Lopez¹³, M. Urbani¹³ & A. Santos¹⁴

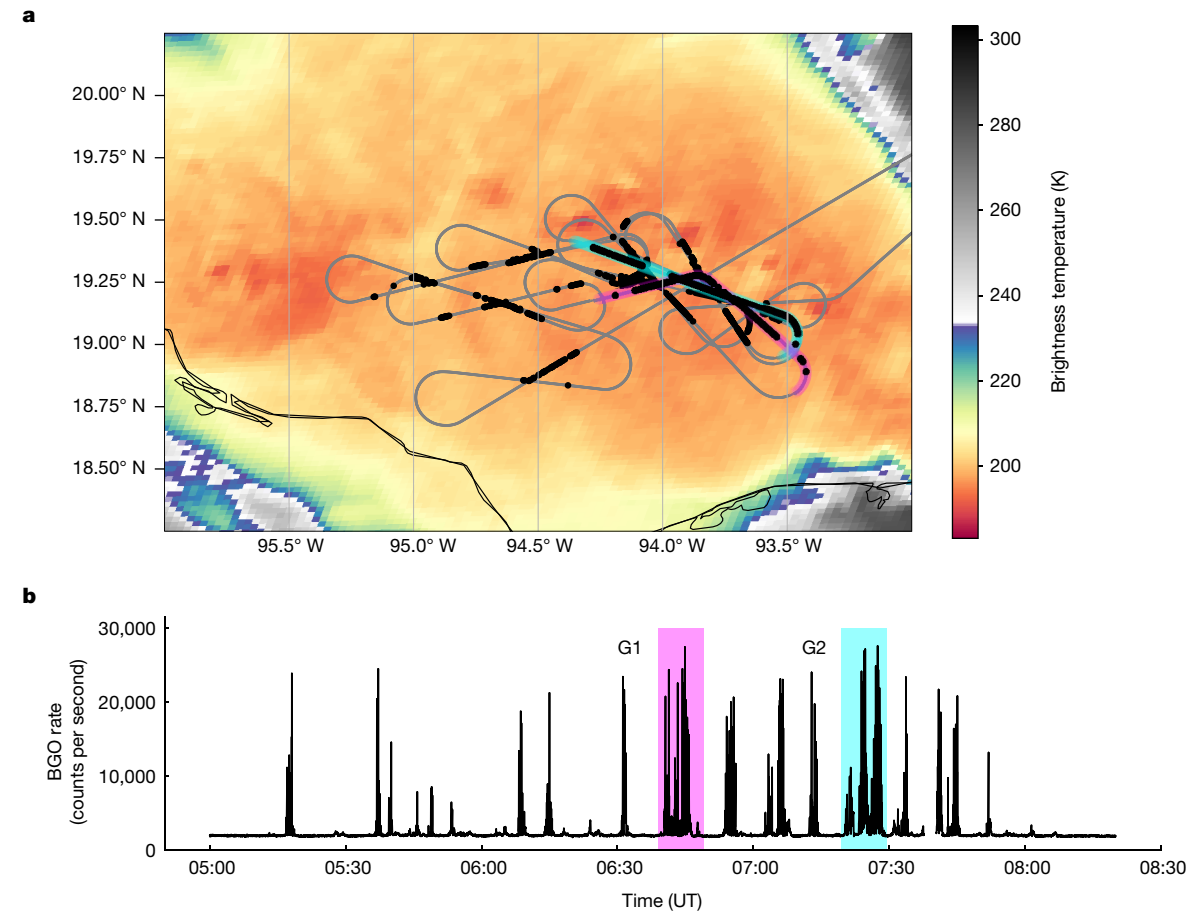
Thunderstorms emit fluxes of gamma rays known as gamma-ray glows^{1,2}, sporadically observed by aircraft^{1,3-7}, balloons⁸⁻¹¹ and from the ground¹²⁻¹⁸. Observations report increased gamma-ray emissions by tens of percent up to two orders of magnitude above the background, sometimes abruptly terminated by lightning discharges^{1,3-5}. Glows are produced by the acceleration of energetic electrons in high-electric-field regions within thunderclouds⁸ and contribute to charge dissipation³. Glows had been considered as quasi-stationary phenomena^{3,5,12}, with durations up to a few tens of seconds and spatial scales up to 10-20 km. However, no measurements of the full extension in space and time of a gamma-ray-glow region and their occurring frequency have been reported so far. Here we show that tropical thunderclouds over ocean and coastal regions commonly emit gamma rays for hours over areas up to a few thousand square kilometres. Emission is associated with deep convective cores; it is not uniform and continuous but shows characteristic timescales of 1-10 s and even subsecond for individual glows. The dynamics of gamma-glowing thunderclouds strongly contradicts the quasi-stationary picture of glows and instead resembles that of a huge gamma-glowing 'boiling pot' in both pattern and behaviour.

During the Airborne Lightning Observatory for FEGS and TGFs (ALOFT) aircraft campaign over the Caribbean and Central America in the summer of 2023, the simplistic picture of localized and uniformly gamma-ray-glowing thunderclouds was overridden. Owing to a new mission concept, in which 1-s-resolution data were downlinked during flight, gamma-ray-glowing clouds could be identified in real time and the pilot was instructed to return to the same location until the thundercloud stopped glowing. ALOFT detected more than 5001-10-s-long individual gamma-ray glows during nine of the ten flights, all over ocean or coastal regions (see Extended Data Table 1), showing that thunderclouds can emit gamma rays for hours and over huge regions.

Figure 1a shows the flight path on 24 July 2023 above a very active mesoscale convective system over southern Campeche Bay. Glows with fluxes up to about 12 times the background level (on 1-s timescales) were detected during almost all of the 3 h spent on target (Fig. 1b). Glows were detected repeatedly following consecutive passages over the same thundercloud system (see crossing trajectories and black dots in Fig. 1a). The overall region including the cyan and magenta trajectories in Fig. 1a was glowing for at least the 3 h we stayed on target, starting at 05:15 UT. We do not know whether the thundercloud was glowing before we arrived and after we had to leave. The glowing region corresponds to an area of more than 9.000 km².

Our glow observations show notable temporal variability down to the 10-ms timescale, overriding the previous picture of quasi-steady smoothly varying glows. Figure 2 shows successively zoomed-in observations of the gamma-ray count rate during an 8-min-long pass and glow sequence, labelled G1 and highlighted in magenta in Fig. 1 (about 100 km aircraft flight distance). Figure 2c,e shows the individual few-second-long glows (<2 km aircraft flight distance). Figure 2f shows a 'glow burst' with brightening by a factor of about 3 over 20 ms, followed by a gradual flux reduction to the previous level on the same timescale. On a 1-ms timescale, this corresponds to an enhancement above the background by a factor of about 30. A duration of a few tens of milliseconds is three orders of magnitude lower than the typical duration of glows reported from previous observations (tens of seconds to minutes), yet is much longer than that of terrestrial gamma-ray flashes (TGFs) (roughly 10–100 μs), which are bright, very short transients usually associated with lightning discharges 19-22. Transients tens of milliseconds long have been presented 23 and have been related to positron clouds. The glow burst presented here does not show any evidence for an

Department of Physics and Technology, University of Bergen, Bergen, Norway. 2Astrophysics and Space Science Observatory of Bologna, National Institute for Astrophysics, Bologna, Italy. 3NASA Marshall Space Flight Center, Huntsville, AL, USA. 4U.S. Naval Research Laboratory, Washington, DC, USA. 5NASA Goddard Space Flight Center, Greenbelt, MD, USA. 6New Mexico Institute of Mining and Technology, NM, Socorro, USA. 7Department of Atmospheric Science, Earth System Science Center, University of Alabama in Huntsville, Huntsville, AL, USA. 8Universities Space Research Association, Huntsville, AL, USA, 9Duke University, Durham, NC, USA, 10Instituto de Ciencias de la Atmósfera y Cambio Climático, National Autonomous University of Mexico (UNAM), Mexico City, Mexico. 11University of Bath, Bath, UK. 12Georgia Institute of Technology, Atlanta, GA, USA. 13Polytechnic University of Catalonia, Barcelona, Spain. 14Universidad Nacional de Colombia, Bogotá, Colombia, Ee-mail: Martino, Marisaldi@uib, no: Nikolai, Ostgaard@uib, no: Andrev, Mezentsev@uib, no



 $\label{lem:fig.1} \textbf{Map and gamma-ray sequence for the flight on 24 July 2023.} \ a, \textbf{Flight} trajectory (grey) overlaid on GOES-18 infrared temperatures, along with marked gamma-ray fluxes exceeding 25% above the background level (black dots). The magenta trajectory corresponds to the glowepisodes plotted in Fig. 2b, also marked as G1 in panel$ **b**. The cyan trajectory corresponds to the glow episodes

plotted in Fig. 3, also marked as G2 in panel ${\bf b}$. For both trajectories, the direction of motion of the plane is from left to right. The brightness temperature cloud image corresponds to time 07:24:251 UT, close to the maximum emission in the cyan region. ${\bf b}$, BGO count rate. Time on target: 05:00–08:20 UT.

enhanced positron annihilation line at 511 keV (see spectral analysis in Methods section 'Glow spectral analysis' and Extended Data Fig. 9b) and therefore must be considered as a new phenomenon. Figure 2d shows another glow that evolved into repetitive behaviour termed a flickering gamma-ray flash (FGF)²⁴, in which the intensity is modulated in a succession of millisecond-duration spikes, separated by tens of milliseconds. Both the occurrence of FGFs and glow bursts lasting only a few tens of milliseconds contradict the canonical picture of glows as quasi-static phenomena well separated from the very short transient TGFs, rather suggesting a more complex scenario linking these two phenomena.

Figure 3 shows how the glow episodes of a typical pass (in this case, the cyan-highlighted episode G2 in Fig. 1) are related to the stormstructure, as determined by the planar cloud-top brightness temperature (Fig. 3b) and the vertical reflectivity profile (Fig. 3c). Together, the observations clearly indicate three convective cores producing high radar reflectivity, each 20–25 km in horizontal extent, with cloud tops extending up to approximately 16.5 km altitude. This implies large liquid and ice contents as well as strong convective updrafts at high altitudes in the cores. The upward-pointing electric field vectors (Fig. 3c) are consistent with the charge structure of thunderclouds typically having an upper positive charge layer, which is also supported by ground observations for the flight on 29 July 2023 over Florida (see Methods section 'Flight on 29 July 2023: comparison with lightning activity and storm charge structure' and Extended Data Figs. 5 and 6).

The above correlations pertain to episode G2 of the 24 July 2023 observations, but similar correlations are obtained for episode G1 and overflights of other storms, as seen in Extended Data Fig. 2 for

an earlier 6 July 2023 Campeche Bay storm and Extended Data Fig. 4 for the 29 July 2023 Florida storm. In each case, the gamma-ray-glow activity is markedly temporally aligned with the overpass of successive cores, with an overall modulation in maximum intensity qualitatively consistent with the cloud-top altitude. Gamma-ray episodes over cores consisted of several (up to a few tens) individual glows, often partially overlapping. The temporal profile of individual glows is typically asymmetric, with a slow rise lasting a few seconds and a fast decay (<1 s). This scenario is a common pattern observed throughout the campaign (nine of ten flights); see Methods section 'Duration and extension of gamma-ray-glow activity'. Each glow episode (a passage over a convective core, encompassing many individual glows) is also accompanied by an increase in the local rate of electrical discharges detected by the Electric Field Change Meter (EFCM) (see Extended Data Figs. 2 and 4 and Methods section 'Instrumentation').

To summarize, we can state with certainty that a thundercloud region can glow for hours and extend over several thousands of square kilometres. The longest continuous enhancement previously reported is 40 min (ref. 25), but this was only a 2% increase above background over a 1-min time bin, not even close to or comparable with the glows we report here with increases of 10-30 times the background. We can also state that each glowing episode typically lasts for about $2 \min (20-25 \text{ km}$ aircraft flight distance). For the individual glows (1 to about 10 s duration), however, we cannot disentangle the spatial and temporal variability components from gamma-ray observations, therefore we cannot establish the physical extent of the single-source regions, whether they cover the full extent of the convective cores or if they are more

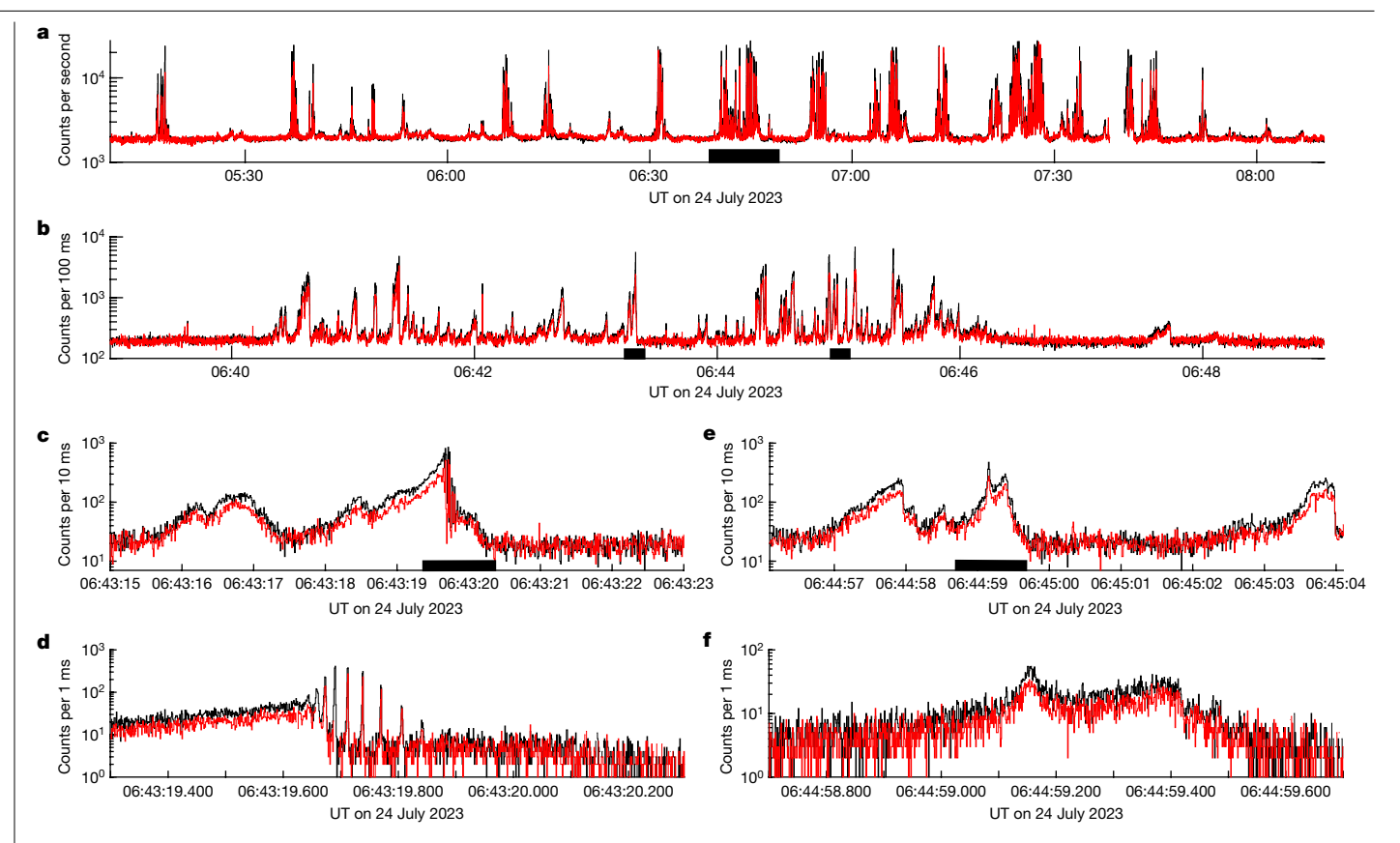


Fig. 2 | Gamma-ray-glow temporal variability. a, BGO (black) and iSTORM (red) count rates (1-s bin) for 24 July 23. **b**, Zoomed view (100-ms bin) for the 10-min time interval highlighted in black in panel **a**, corresponding to time

 $interval\,G1\,highlighted\,in\,magenta\,in\,Fig.\,1.\,\textbf{c,e}, Zoomed\,view\,(10\text{-ms}\,bin)\,for\,the$ 8-s time intervals highlighted in black in panel **b**. **d**, **f**, Zoomed view (1-ms bin) for the 1-s time intervals highlighted in black in panels \mathbf{c} and \mathbf{e} , respectively.

compact regions within the cores. Monte Carlo simulations suggest an effective range for glow observations of 2.0 to about 4.5 km, depending on production altitude (see Methods section 'Attenuation with radial distance' and Extended Data Fig. 7). Therefore, active regions must be located within the cores. The typical rise time (2-4 s) and fall time (<1 s) of individual glows are too short compared with the characteristic times

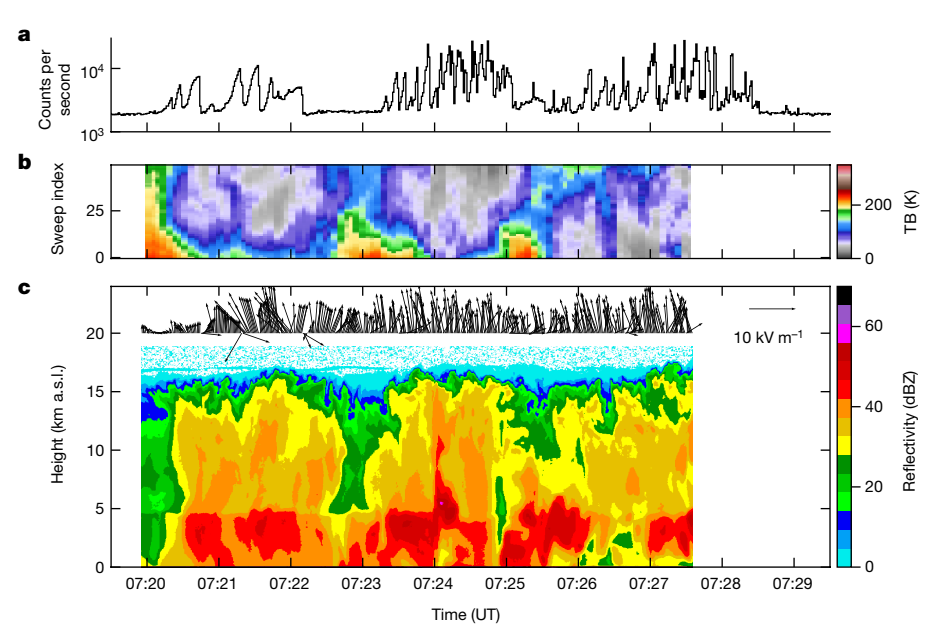


Fig. 3 | Sequence of glows with simultaneous electric-field and cloudcharacterization data. Time interval G2 on 24 July 2023 highlighted in cyan in Fig. 1. a, BGO count rate. b, Brightness temperature (TB) from the Advanced Microwave Precipitation Radiometer (AMPR) 85.5 GHz Channel A. Sweep index 0 (49) corresponds to scan direction 45° from nadir towards starboard (port). c, Vertical radar reflectivity profile from the X-band

radar (EXRAD). Black vectors are the E_{xz} component of the electric field from the Lightning Instrument Package (LIP), in which the x axis is the direction of motion and the z axis is the upward-pointing vertical direction. AMPR, EXRAD and LIP (see Methods section 'Instrumentation') data are not shown if the roll $angle\,is\,larger\,than\,2^{\circ}\,(aircraft\,man oeuvring).\,a.s.l., above\,sea\,level.$

expected from aircraft motion towards a stationary source (see Methods section 'Time profile resulting from aircraft motion' and Extended Data Fig. 8). Therefore, the temporal dynamics of individual glows is most likely dominated by the intrinsic time variability of the gamma-ray emission, which reflects the variability of the underlying electric field. We expect the rise time of glows to be associated with electric-field increase owing to convection-driven charge build-up and the shorter fall time to be associated with electric-field reduction owing to charge removal following discharge processes.

In most cases, a glow flux reduction does not bring the observed flux down to the background level but rather to an intermediate level immediately followed by a new rise phase (Fig. 2c,e). We cannot state whether this is because of a partial discharge followed by a recharging of the same active region or by the superposition of fluxes coming from nearby active regions within the same core. The overall time profile of glow episodes, with the brightest glows typically observed passing over the centre of the convective cores (see Fig. 3), suggests that most of the gamma rays do not come from a large-scale, core-sized active region but rather from one or more compact regions concentrated towards the centre of the cores. For the subsecond glow bursts with only tens of millisecond rise and fall times, we can—with high confidence—state they are the result of temporal variability of the source region.

The observations suggest what we call 'the boiling pot analogy'. Gamma-ray-glowing regions are tightly associated to strong convective cores, with several individual cores evolving during the development and mature phases of tropical thunderstorms. Local gamma-ray emission follows the lifetime of the associated core, but particularly with large multicell storms, the overall gamma-ray-glowing region can last for hours and extend over thousands of square kilometres, tightly matching the most active regions of the storm.

So far, modelling efforts have been on the basis of simplistic assumptions on the extent of the glow region and electric-field configurations 26,27 , namely uniform and constant electric field extended over large (several square kilometres) regions. Our observations prompt the need to go beyond this simplistic static representation of glows. Inhomogeneous charge structure and its temporal dynamics must be considered in realistic simulations. The pervasiveness of gamma-ray emission over large time and spatial scales in ocean and coastal tropical thunderclouds has a broad range of implications, barely touched on in previous studies, ranging from their effects on cloud discharge³, alteration of the local environment owing to isotope production²⁸ and potential effect on cloud chemistry and dynamics.

Online content

Any methods, additional references, Nature Portfolio reporting summaries, source data, extended data, supplementary information, acknowledgements, peer review information; details of author contributions and competing interests; and statements of data and code availability are available at https://doi.org/10.1038/s41586-024-07936-6.

- Parks, G. K. et al. X-ray enhancements detected during thunderstorm and lightning activities. Geophys. Res. Lett. 8, 1176-1179 (1981).
- Dwyer, J. R., Smith, D. M. & Cummer, S. A. High-energy atmospheric physics: terrestrial gamma-ray flashes and related phenomena. Space Sci. Rev. 173, 133-196 (2012).
- Kelley, N. A. et al. Relativistic electron avalanches as a thunderstorm discharge competing with lightning. Nat. Commun. 6, 7845 (2015).
- Ostgaard, N. et al. Gamma ray glow observations at 20-km altitude. J. Geophys. Res. Atmos. 124, 7236-7254 (2019).
- Kochkin, P. et al. In-flight observation of gamma ray glows by ILDAS. J. Geophys. Res. Atmos. 122, 12801-12811 (2017).
- McCarthy, M. & Parks, G. K. Further observations of X-rays inside thunderstorms Geophys. Res. Lett. 12, 393-396 (1985).
- McCarthy, M. P. & Parks, G. K. On the modulation of X ray fluxes in thunderstorms. J. Geophys. Res. Atmos. 97, 5857-5864 (1992).
- Eack, K. B. & Beasley, W. H. Long-duration X-ray emissions observed in thunderstorms. J. Geophys. Res. Atmos. 120, 6887-6897 (2015).
- Eack, K. B. et al. X-ray pulses observed above a mesoscale convective system. Geophys. Res. Lett. 23, 2915-2918 (1996).
- Eack, K. B. et al. Initial results from simultaneous observation of X rays and electric fields in a thunderstorm, J. Geophys. Res. Atmos. 101, 29637-29640 (1996).
- Eack, K. B. et al. Gamma-ray emissions observed in a thunderstorm anvil. Geophys, Res. Lett. 27, 185-188 (2000).
- Wada, Y. et al. Catalog of gamma-ray glows during four winter seasons in Japan. Phys. Rev. Res. 3, 043117 (2021).
- 13. Chilingarian, A. Thunderstorm ground enhancements—model and relation to lightning flashes. J. Atmos. Sol. Terr. Phys. 107, 68-76 (2014).
- Chilingarian, A., Mailyan, B. & Vanyan, L. Recovering of the energy spectra of electrons and gamma rays coming from the thunderclouds. Atmos. Res. 114-115, 1-16 (2012).
- Chilingarian, A., Hovsepyan, G. & Hovhannisyan, A. Particle bursts from thunderclouds: natural particle accelerators above our heads. Phys. Rev. D 83, 062001 (2011).
- Chilingarian, A., Hovsepyan, G. & Vanyan, L. On the origin of the particle fluxes from the thunderclouds: energy spectra analysis. Europhys. Lett. 106, 59001 (2014).
- Tsuchiya, H. et al. Hardening and termination of long-duration y rays detected prior to lightning. Phys. Rev. Lett. 111, 015001 (2013).
- Tsuchiya, H. et al. Long-duration y ray emissions from 2007 and 2008 winter thunderstorms. J. Geophys. Res. Atmos. 116, D09113 (2011).
- Smith, D. M. et al. Terrestrial gamma-ray flashes observed up to 20 MeV. Science 07. 1085-1088 (2005).
- Marisaldi, M. et al. Detection of terrestrial gamma ray flashes up to 40 MeV by the AGILE 20 satellite, J. Geophys, Res. Space Phys. 115, A00E13 (2010).
- Briggs, M. S. et al. First results on terrestrial gamma ray flashes from the Fermi Gammaray Burst Monitor, J. Geophys, Res. Space Phys. 115, A07323 (2010).
- Ostgaard, N. et al. First 10 months of TGF observations by ASIM, J. Geophys, Res. Atmos. **124**. 14024-14036 (2019).
- Dwyer, J. R. Positron clouds within thunderstorms, J. Plasma Phys. 81, 475810405 (2015)
- Østgaard, N. et al. Flickering gamma-ray flashes, the missing link between gamma glows and TGFs. Nature https://doi.org/10.1038/s41586-024-07893-0 (2024).
- Tsuchiva, H. et al. Observation of thundercloud-related gamma rays and neutrons in Tibet. Phys. Rev. D 85, 092006 (2012).
- Sarria, D. et al. Library of simulated gamma-ray glows and application to previous airborne observations. J. Geophys. Res. Atmos. 128, e2022JD037956 (2023).
- Wada, Y. et al. Negative excursion of surface electric fields during gamma-ray glows in winter thunderstorms. J. Geophys. Res. Atmos. 128, e2023JD039354 (2023)
- Enoto, T. et al. Photonuclear reactions triggered by lightning discharge. Nature 551, 481-484 (2017).

Publisher's note Springer Nature remains neutral with regard to jurisdictional claims in published maps and institutional affiliations.

Springer Nature or its licensor (e.g. a society or other partner) holds exclusive rights to this article under a publishing agreement with the author(s) or other rightsholder(s); author self-archiving of the accepted manuscript version of this article is solely governed by the terms of such publishing agreement and applicable law.

© The Author(s), under exclusive licence to Springer Nature Limited 2024

Methods

The ALOFT flight campaign

The Airborne Lightning Observatory for FEGS (Fly's Eye GLM Simulator, in which GLM stands for Geostationary Lightning Mapper) and TGFs (ALOFT) is an aircraft campaign conducted during the month of July 2023 with a NASA ER-2 aircraft based at the MacDill Air Force Base in Tampa, Florida, USA. A total of ten flights (3–8 h each) at 20-km altitude were performed. Each flight spent 3–4 h above active thunderstorms. Extended Data Table 1 shows an overview of the flight dates, durations, target locations and total number of observed glow episodes and gamma-ray glows.

The science goals of ALOFT were the observation of TGFs and gamma-ray glows from thunderstorms and the study of their connection. The airborne scientific payload consists of five independent gamma-ray detectors, 30 photometers, three electric-field sensors, two radars and two passive radiometers. Also, nine ground-based radio receivers were operated during the campaign, covering very low frequencies, low frequencies (LF) and very high frequencies, including two interferometers and one Lightning Mapping Array (LMA). The instruments used in this study are described in Methods section 'Instrumentation'.

A key feature of the mission was the near-real-time downlink of 1-s time resolution gamma-ray count rates. This enabled the immediate identification of gamma-ray-glowing thunderclouds and the pilot was instructed to return to the same location as long as gamma-ray glows were detected.

Instrumentation

The Bismuth-Germanium-Oxide instrument from the University of Bergen (UIB-BGO). This instrument consists of four independent gamma-ray detectors; one bismuth germanium oxide (BGO) detector, with three independent BGO crystals with photomultiplier tube (PMT) readout, and three LYSO detectors. All detectors have different geometric areas ranging from 0.09 to 225 cm², to provide four orders of magnitude dynamic range in flux. In fact, modelling work²⁹ showed that the flux from a typical TGF observed at 20-km altitude can vary by four orders of magnitude, depending on the radial distance from the source to the aircraft. The three BGO/PMT detectors are similar in design and readout architecture to one of the four High-Energy Detector modules of the Modular X- and Gamma-ray Sensor (MXGS)³⁰ aboard the Atmosphere-Space Interactions Monitor (ASIM) on the International Space Station (ISS). The three BGO/PMT detectors have a total geometrical area of 225 cm², are sensitive in the energy range 300 keV to > 30 MeV and have a 28-ns time-tagging accuracy. In this work, we use only data from the BGO detectors. Further information on UIB-BGO can be found in the companion paper²⁴.

The in-Situ Thunderstorm Observer for Radiation Mechanisms (iSTORM). iSTORM is a gamma-ray spectrometer designed and built by the U.S. Naval Research Laboratory for the measurement of bright, fast transients in the energy range approximately 300 keV to >5 MeV). iSTORM consists of an array of 32 1-inch-diameter CeBr $_3$ scintillating crystals with silicon photomultiplier (SiPM) readout, with temporal resolution <1 μ s, for a total geometrical area of 157 cm 2 . The large area provides high sensitivity, whereas the high segmentation and fast scintillation decay time provides robustness towards potential detector paralysis from bright TGFs. Further information on iSTORM can be found in the companion paper 24 .

The Advanced Microwave Precipitation Radiometer (AMPR). The AMPR is a cross-track scanning radiometer that passively measures total power at 10.7 GHz, 19.35 GHz, 37.1 GHz and 85.5 GHz (ref. 31). The instrument uses a rotating splash plate mirror to focus microwave energy into its feedhorns. This causes the polarization of the incoming

signal to vary sinusoidally as a function of scan angle. The AMPR has two orthogonally polarized channels per frequency, so it is possible to retrieve fully vertical and fully horizontal polarizations by deconvolving the orthogonal measurements at each frequency. At ER-2 altitudes, the instantaneous field-of-view resolution of the AMPR varies between 0.6 and 2.8 km, with the finest resolution associated with 85.5 GHz and the coarsest resolution associated with 10.7 GHz. The AMPR's swath is about 38 km wide when flying at 20-km altitude on the ER-2. The AMPR completes a cross-track scan in roughly 2.5 s and, after five scans, the instrument collects measurements of two blackbodies—a heated hot load and an air-cooled cold load—to enable calibrated brightness temperature retrievals.

AMPR brightness temperatures are first retrieved using a simple two-point linear method that compares scene radiometer counts to the radiometer counts from the hot load (typically around 320 K) and from the cold load (which can reach a minimum temperature of about 240 K during a flight). With most meteorological scenes, this methodology is capable of producing well-calibrated brightness temperatures suitable for quantitative geophysical retrievals³¹. However, $during \, the \, ALOFT \, flight \, campaign, it \, was \, found \, that, owing \, to \, the \, large$ amount of ice scattering observed in these storms, a linear assumption was not suitable for the 85-GHz channels, as the scene targets were so radiometrically cold that receiver response entered a nonlinear regime. Thus, AMPR 85-GHz brightness temperatures were corrected for receiver nonlinearity using a simple gain adjustment factor that became stronger as scene counts went lower than cold load counts and thus prevented negative brightness temperature retrievals. This correction also reproduced 85-GHz brightness temperatures that were within approximately ±10 K of previous AMPR observations of intense convection^{32,33} and that remained highly correlated with 85-GHz scene counts (Pearson correlation coefficient > 0.9). The corrected 85-GHz brightness temperatures are thus suitable for qualitative identification of substantial precipitation cores and the presence of ice scattering.

The ER-2 X-band Radar (EXRAD). The EXRAD is an X-band (9.6-GHz) precipitation radar and scatterometer that flies in the ER-2 nose and it is used for measuring both the 3D precipitation structure and surface winds. It has a fixed nadir beam and a conical scanning beam that is tilted approximately 30° off nadir. The EXRAD measures radar reflectivity, Doppler velocity and Doppler spectral width. It was first flown in 2014. The EXRAD uses a 0.66-m-diameter slotted waveguide antenna with a single linear polarization for the scanning beam plus a second 0.66-m linear polarized slotted waveguide antenna for a nadir beam. This approximately 3.4° beam provides a beamwidth of approximately 0.6 km at 10-km altitude and 1.2 km at the surface. EXRAD calibration is performed using the ocean surface and current Doppler processing includes non-uniform beam-filling corrections for artefacts caused by the aircraft motion. Calibration accuracy is better than 1 dBZ for reflectivity and <1 ms⁻¹ for Doppler. More details on the EXRAD hardware and processing can be found in ref. 34.

The Lightning Instrument Package (LIP). The LIP consists of seven rotating-vane electric-field mills installed on the NASA ER-2 aircraft to observe the total vector electric field and vector electric field (E_{xy} , E_z) generated by cloud charging and lightning discharges^{35–38}. The LIP measures the vector electric field in the atmosphere and the charge induced on the aircraft using the processing and calibration technique in ref. 39. The individual laboratory dynamic range for the mills is ± 1.75 V m⁻¹ to 920 kV m⁻¹. Properly calibrated on the aircraft, the LIP can reliably measure fields lower than 1 V m⁻¹ and as high as 512 kV m⁻¹ with 0.1-s temporal resolution. Effects on the derived vertical electric field resulting from aircraft charging are generally 5% or less, with a maximum upper error of 10% (ref. 36). Both aircraft-relative and Earth-relative frameworks are determined, and the total electric-field magnitude is then computed from the vector components.

The Electric Field Change Meter (EFCM). The EFCM is a two-channel (fast and slow) antenna that measures the derivative of the electric-field impulse produced by lightning. The fast channel is designed to isolate the radiative component of the lightning discharge field, whereas the slow channel is optimized to observe the electrostatic-field component. The EFCM has several sensitivity ranges that are selectable during flight and samples with 16-bit resolution. The EFCM trigger rate shown in Extended Data Figs. 2 and 4 is clipped at a maximum of ten triggers in 10 s. This is because an EFCM trigger implies acquisition of 1-s data around the trigger time. Such a rate is therefore the maximum trigger rate possible, implying nearly continuous data recording. The real discharge rate may be much higher. Further information on the EFCM can be found in the companion paper 24 .

The Central Florida Lightning Mapping Array (CFLMA). The CFLMA consisted of six widely spaced very-high frequency (VHF) stations that receive the VHF radiation produced by lightning in a 6-MHz bandwidth between 60 and 66 MHz (US TV Channel 3). Each station detects the peak radiation event above a local threshold value in successive 80-µs time windows with 40-ns time resolution and uses the arrival times at the different sites to locate the sources of impulsive radiation sources in three spatial dimensions and time, as well as the VHF source powers. Owing to logistical and sensitivity issues, a small number of events were detected per flash, but these were sufficient both for obtaining the basic location of individual flashes and for determining the overall electric-charge structure of the storms. Important high-power events were well detected and located by the network.

Advanced Baseline Imager (ABI). This work makes use of public data from the ABI instruments aboard the GOES-16 and GOES-18 geostationary satellites. ABI provides radiometric measurements in 16 spectral bands from the visible (0.47 μ m) to the infrared (13.3 μ m), with spatial resolution from 0.5 km (visible) to about 2 km (infrared). The temporal resolution depends on the ABI operational mode. For seven flights out of ten, the ALOFT mission was granted a dedicated Mesoscale Domain Sector, which provides scans of a 1,000 \times 1,000-km² box every 60 s. For the three flights over Florida, we made use of the Continental US (CONUS) scans, which are provided every 5 min. In this work, we use radiance measurements in the ABI band 13 (infrared, 10.3 μ m), which are then converted to brightness temperatures by applying the Planck function and a spectral bandpass correction according to the GOES-R Series Product Definition and Users' Guide 40 .

Duration and extension of gamma-ray-glow activity

In this section, we present information on two other flights: 6 July 2023 over Campeche Bay and 29 July 2023 over Florida. As well as the very active storm on 24 July 2023, the other two case studies (shown here), as well as the six other storms all show that the new findings of this paper (hour-long durations, large spatial extension of gamma-ray activity, substantial variability on second to millisecond timescales) are also common features in less severe storms.

For all case studies, we present time-based colour-coded maps and gamma-ray sequences (Extended Data Figs. 1 and 3), which provide a visualization of gamma-ray data alternative to that presented in Fig. 1. Here the reader can match a specific glow episode with a position on the map based on the highlight colour. Also, we provide gamma-ray count rate with simultaneous electric-field and cloud-characterization data for selected time intervals (Extended Data Figs. 2 and 4). These figures show the same observation pattern presented in Fig. 3: glow episodes, each of them comprising several individual glows, are observed during the overpass of convective cores with large radar reflectivity, implying large liquid and ice contents, as well as strong convective updrafts at high altitudes. In all cases, the upward-pointing electric-field vectors are consistent with the presence of an upper positive charge layer. Also, Extended Data Figs. 2 and 4 show the EFCM trigger rate, which peaks

during the passage over gamma-ray-active convective cores. EFCM data were not available for the flight on 24 July 2023.

In the following, we report further information for the case-study flights on 6 July and 29 July.

Flight on 6 July 2023. The target area showed developing multicell convection that evolved into a mesoscale convective system at the time of overflight. The area is Campeche Bay, the same as for the flight on 24 July 2023 discussed in the main text. This storm represents a very clean case illustrating the large spatial extension and long duration of a gamma-ray-glowing thundercloud region. Extended Data Fig. 1 shows six consecutive passes over the same core region, each associated with glow episodes (Extended Data Fig. 2). The total time span of these passes is 40 min, which represents a lower limit of the duration of the glow activity. The overall spatial extension of the glowing region is about 600 km².

Flight on 29 July 2023: comparison with lightning activity and storm charge structure. The flight over east-central Florida on 29 July produced observations similar to those obtained over the Central America coastal areas but included important observations of VHF radiation from the 3D CFLMA over the area. The Florida storm cells were more localized than those of the other flights and produced relatively well-separated glows, as seen in Extended Data Figs. 3 and 4. Extended Data Figs. 3 shows seven consecutive passes over the same approximately 400-km² core region, each of them resulting in notable glow episodes, for a total duration of about 1 h.

The strongest episode occurred at 20:30:30 UT (Extended Data Fig. 3b) and is shown in detail in Extended Data Fig. 5, which compares the glow sequence with LMA observations of the lightning activity. The episode consisted of three glows, the last one much dimmer than the others. Here we focus on the first two glows, each of which was rapidly quenched at the time of an intracloud lightning flash in the storm. The glows were noticeably different from each other, with the first glow lasting 8 s and being detected as the ER-2 entered the periphery of the electrically active storm from the northeast (top horizontal arrow in Extended Data Fig. 5c). By contrast, and by sheer chance, the second glow occurred 20 s later, when the ER-2 was directly above the central part of the storm and the flash that terminated the glow. Instead of increasing linearly with time, as in the first glow, the second glow grew exponentially for 4 s to twice the count rate of the first glow (namely to about 20,000 per second), at which point a highly energetic intracloud flash was initiated that quenched the glow (red sources in the panels of Extended Data Fig. 5, with the ER-2 location indicated by the bottom horizontal arrow in Extended Data Fig. 5c). That the quenching flash was energetic is indicated by two of the initial LMA sources having extremely strong VHF powers of 53.9 and 52.9 dBW, or about 200 kW. (The quenching flash for the first glow had moderate source powers and corresponded to the light-green sources in the same plan area and altitude range as the subsequent red sources in Extended Data Fig. 5c).

Extended Data Fig. 6 shows the lightning-inferred charge structure around the time of the 20:30 glows, showing that the storm had a normal-polarity tripolar structure, with upper positive charge between about 13 and 15 km and mid-level negative charge at about 9–12 km, and confirming that the first glow was observed on the periphery of both charge regions, whereas the second glow was observed directly above the core. The polarity is inferred by virtue of intracloud flashes producing higher-power RF-noisy negative-polarity breakdown through the upper positive charge of the storm and less noisy positive breakdown within the mid-level charge of the storm 41 .

Monte Carlo simulations

Using Monte Carlo simulations, we can evaluate certain theoretical characteristics of gamma-ray glows. It is anticipated that all observed

spectra originate from the relativistic runaway electron avalanche (RREA) process. We used the Geant4 software 42 , which enables the simulation of photon, electron and positron propagation in the atmosphere. The simulation initiates with a point source of upward-pointing electrons, with a classical RREA energy spectrum up to 40 MeV at the source 43 . The simulations follow these steps: (1) propagation, scattering and absorption of RREA electrons in the atmosphere, along with the generation and propagation of secondary Bremsstrahlung photons from various altitudes (ranging from 8 to 16 km); (2) the recording of photons at an altitude of 20 km, which corresponds to the altitude of the aircraft; (3) these point-source simulations are extended by random sampling to generate any extended source.

Attenuation with radial distance. Here we estimate how far away from the aircraft nadir can gamma-ray glows be detected by ALOFT. We can safely identify dim glows that exhibit a minimum count rate increase of 25% above the background level (using 1-s time bin). Conversely, the brightest glows exhibit a count rate up to about 12 times the background (using 1-s time bin). We therefore detect glows with maximum intensity spanning a dynamic range of about 50. This observed dynamic range includes both contributions from the intrinsic glow intensity variability and absorption owing to the source location with respect to the aircraft. Extended Data Fig. 7 shows the expected number of photons per unit area at 20-km altitude for sources at different altitudes and radial distance from the aircraft, normalized to 1 at radial distance 0. The dashed horizontal line marks the detection threshold (0.02, following from a dynamic range of 50). Assuming that the brightest glows are detected from sources close to the nadir, we can see that a source as bright would be detectable at 25% above the background level up to roughly 2.0-4.5-km radial distance, depending on the source altitude. Considering that glows are detected while passing over convective cores extending at high altitudes, it is likely that the sources have a high altitude as well (see discussion of the cloud-charge structure in Methods section 'Flight on 29 July 2023: comparison with lightning activity and storm charge structure'), therefore the detection range is probably lower than about 3.5 km.

Time profile resulting from aircraft motion. Here we estimate the observed time profile of a stationary gamma-ray glow resulting only from the aircraft motion. Extended Data Fig. 8 shows the relative number of counts at aircraft altitude assuming that the aircraft is flying towards an extended source (7.5-km radius disk) at 16-km altitude for different radial offsets. The rise time from 2% (detection threshold assuming the dynamic range 50 discussed in Methods section 'Attenuation with radial distance') to 95% of the maximum is >18 s. This is much longer than the typically observed rise times (2–4 s), suggesting that the intrinsic time variability of the source dominates the observed time profile. This rise time further increases with increasing radial offset from the source. The relative intensity sharply decreases when the radial offset exceeds the physical extension of the glow region, in agreement with the attenuation with radial distance discussed above in Methods section 'Attenuation with radial distance'.

Glow spectral analysis. Here we show that the energy spectra of a sample of the detected gamma-ray glows can be well modelled by the RREA process. Extended Data Fig. 9a presents energy spectra and light curves for four cases detected during the flight on 6 July 2023. It also includes the best-fit results from a RREA model, which closely matches the observed glow spectra. The fitting procedure involved the following steps:

- Start with an upward electron source at 15-km altitude, with a typical RREA electron energy spectrum.
- Propagating these electrons through the atmosphere and recording Bremsstrahlung photons at 20-km altitude (only a negligible fraction of electrons reach this altitude).

3. Applying the response matrix of the BGO instrument to simulate the spectrum and subsequently comparing it with the observed data.

For the best fit, we used an averaged spectrum derived from all the observations shown. A key parameter optimized in this modelling was the extent of the RREA region. The best fit was achieved with a source region larger than 8-km spatial extent, determined using a maximum-likelihood approach. Although the approach is potentially mixing sources with different characteristics, it shows that the RREA process is a good explanation for the observed gamma-ray-glow spectra.

With the same procedure, we also performed spectral analysis of the glow burst detected on 24 July 2024 at 06:44:59.182 UT and presented in Fig. 2f. Extended Data Fig. 9b presents the energy spectrum for this event. The spectrum can be well fit with a RREA model and does not show any evidence of enhanced features at the 511-keV positron annihilation line. Therefore, we conclude that this event is intrinsically different from the positron bursts presented in ref. 23.

Data availability

All the data used in this study are available on the Zenodo repository at https://doi.org/10.5281/zenodo.12531291 (ref. 44). The description of the formats is uploaded in the file Data_description.pdf.

Code availability

References to software tools and codes for this study are given in the file Data_description.pdf, which is uploaded to the Zenodo repository at https://doi.org/10.5281/zenodo.12531291 (ref. 44).

- 29. Hansen, R. S. et al. How simulated fluence of photons from terrestrial gamma ray flashes at aircraft and balloon altitudes depends on initial parameters. *J. Geophys. Res. Space Phys.* 118, 2333–2339 (2013)
- Østgaard, N. et al. The Modular X- and Gamma-Ray Sensor (MXGS) of the ASIM payload on the International Space Station. Space Sci. Rev. 215, 23 (2019).
- Amiot, C. G. et al. Dual-polarization deconvolution and geophysical retrievals from the Advanced Microwave Precipitation Radiometer during OLYMPEX/RADEX. J. Atmos. Ocean. Technol. 38, 607–628 (2021).
- Leppert, K. D. & Cecil, D. J. Signatures of hydrometeor species from airborne passive microwave data for frequencies 10–183 GHz. J. Appl. Meteorol. Climatol. 54, 1313–1334 (2015).
- Battaglia, A. et al. Using a multiwavelength suite of microwave instruments to investigate the microphysical structure of deep convective cores. J. Geophys. Res. Atmos. 121, 9356–9381 (2016)
- Heymsfield, G. M. et al. in Advances in Weather Radar Vol. 1 (eds Bringi, V. N., Mishra, K. V. & Thurai, M.) 231–282 (Institution of Engineering and Technology, 2024).
- Bateman, M. G. et al. A low-noise, microprocessor-controlled, internally digitizing rotating-vane electric field mill for airborne platforms. J. Atmos. Ocean. Technol. 24, 1245–1255 (2007).
- Mach, D. M., Blakeslee, R. J., Bateman, M. G. & Bailey, J. C. Electric fields, conductivity, and estimated currents from aircraft overflights of electrified clouds. *J. Geophys. Res. Atmos.* 114. D10204 (2009).
- Mach, D. M., Blakeslee, R. J., Bateman, M. G. & Bailey, J. C. Comparisons of total currents based on storm location, polarity, and flash rates derived from high-altitude aircraft overflights. J. Geophys. Res. Atmos. 115, D03201 (2010).
- Schultz, C. J. et al. Remote sensing of electric fields observed within winter precipitation during the 2020 Investigation of Microphysics and Precipitation for Atlantic Coast-Threatening Snowstorms (IMPACTS) field campaign. J. Geophys. Res. Atmos. 126, e2021JD034704 (2021).
- Mach, D. M. & Koshak, W. J. General matrix inversion technique for the calibration of electric field sensor arrays on aircraft platforms. J. Atmos. Ocean. Technol. 24, 1576–1587 (2007).
- National Oceanic and Atmospheric Administration (NOAA) & National Aeronautics and Space Administration (NASA). GOES-R Series Product Definition and Users' Guide (PUG), 27–28 (NOAA & NASA, 2019).
- Thomas, R. J. et al. Observations of VHF source powers radiated by lightning. Geophys. Res. Lett. 28, 143–146 (2001).
- Agostinelli, S. et al. Geant4—a simulation toolkit. Nucl. Instrum. Methods Phys. Res. A 506, 250–303 (2003).
- Dwyer, J. R. A fundamental limit on electric fields in air. Geophys. Res. Lett. 30, 2055 (2003).
- Marisaldi, M. Data used in the study: Highly dynamic gamma-ray emissions are common in tropical thunderclouds. Zenodo https://doi.org/10.5281/zenodo.12531291 (2024).

Acknowledgements This work made use of data from UIB-BGO, iSTORM, EXRAD, AMPR, LIP and EFCM from the ALOFT instrument suite, very-high-frequency data from the Central Florida Lightning Mapping Array (CFLMA) and Advanced Baseline Imager data from the GOES-16 and GOES-18 geostationary satellites. The ALOFT campaign and the UIB-BGO instrument was supported by European Research Council under the European Union's Seventh Framework Programme (FP7/2007-2013)/ERC grant agreement no. 320839 and the Research Council of Norway under contracts 223252/F50 (CoE) and 325582. Some of the simulations were performed on resources provided by UNINETT Sigma2—the National Infrastructure for High Performance Computing and Data Storage in Norway, under project no. NN9526K. Work at the U.S. Naval Research Laboratory (NRL) on ALOFT is supported by the Office of Naval Research 6.1 funds. Also, D. Shy is supported by the NRL's Jerome and Isabella Karle Fellowship. The New Mexico Tech authors acknowledge NSF grants 1720600 and 2214044, R. Brown of the University of Central Florida for setting up and operating the CFLMA stations and W. Rison for providing the data. The participation of J.A.R., J.A.L., M.U., O.v.d.V. and J.M. and the fielding of instruments on San Andrés island was supported by projects EQC2021-006957-P and PID2022-136348NB-C33 by the government of Spain (MCIN/AEI/10.13039/501100011033) and the European Regional Development Fund 'ERDF - A way of making Europe' by the European Union, M.F. was sponsored by the Royal Society (UK) grant NMG/R1/180252 and the Natural Environment Research Council (UK) under grants NE/L012669/1 and NE/H024921/1. S.C. and Y.P. were partly supported by the National Science Foundation Dynamic and Physical Meteorology programme through grant no. AGS-2026304. We thank the NASA ER-2 Project Team at NASA Armstrong Flight Research Center for supporting the ALOFT campaign and the MacDill Air Force Base for hosting. Notable financial and logistical support for ALOFT was provided by the NASA Earth Science Division. We thank the governments of Mexico, Bahamas, Colombia, Belize, Guatemala, Honduras, Nicaragua, Panama, Dominican Republic, Costa Rica,

El Salvador, Haiti, Turks and Caicos, Jamaica and the Cayman Islands for approving ER-2 overflights in support of ALOFT. GCES Mesoscale Domain Sectors in support of ALOFT were enabled by NOAA. The FEGS and EFCM team acknowledge the work of S. Podgorny, D. Corredor and M. Stewart. For AMPR, we thank D. Huie (UAH), C. Amiot (NASA Postdoctoral Program) and E. Cantrell (NASA MSFC). We acknowledge the High Altitude Radar Group at NASA Goddard that provided data, including M. McLinden, L. Li, P. Pantina and C. Helms.

Author contributions M.M., N.Ø. and A.M. have led this study. The ALOFT campaign was led by N.Ø., T.L., M.M. and C.S. The UIB-BGO instrument was provided by N.Ø., M.M., K.U., S.Y., B.H.Q., J.S. and B.H. and analysed by A.M., N.Ø., M.M., D. Sarria and N.L. The iSTORM data were provided and analysed by J.E.G., D. Shy and D.W. The AMPR data were provided by T.L. The EXRAD data were provided by G.M.H. The LIP data were provided by C.S., D.M. and M.B. The EFCM data were provided by H.C. and R.B. The CFLMA data were analysed by P.K., R.J.T. and M.S. Further radar and radiometric data for the entire campaign were provided by I.A. and R.K. Further ground radio stations were operated for the entire campaign by S.C., Y.P., M.P., P.B., M.F., M.C., J.M., C.Y., O.v.d.V., J.A.R., J.A.L., M.U. and A.S.

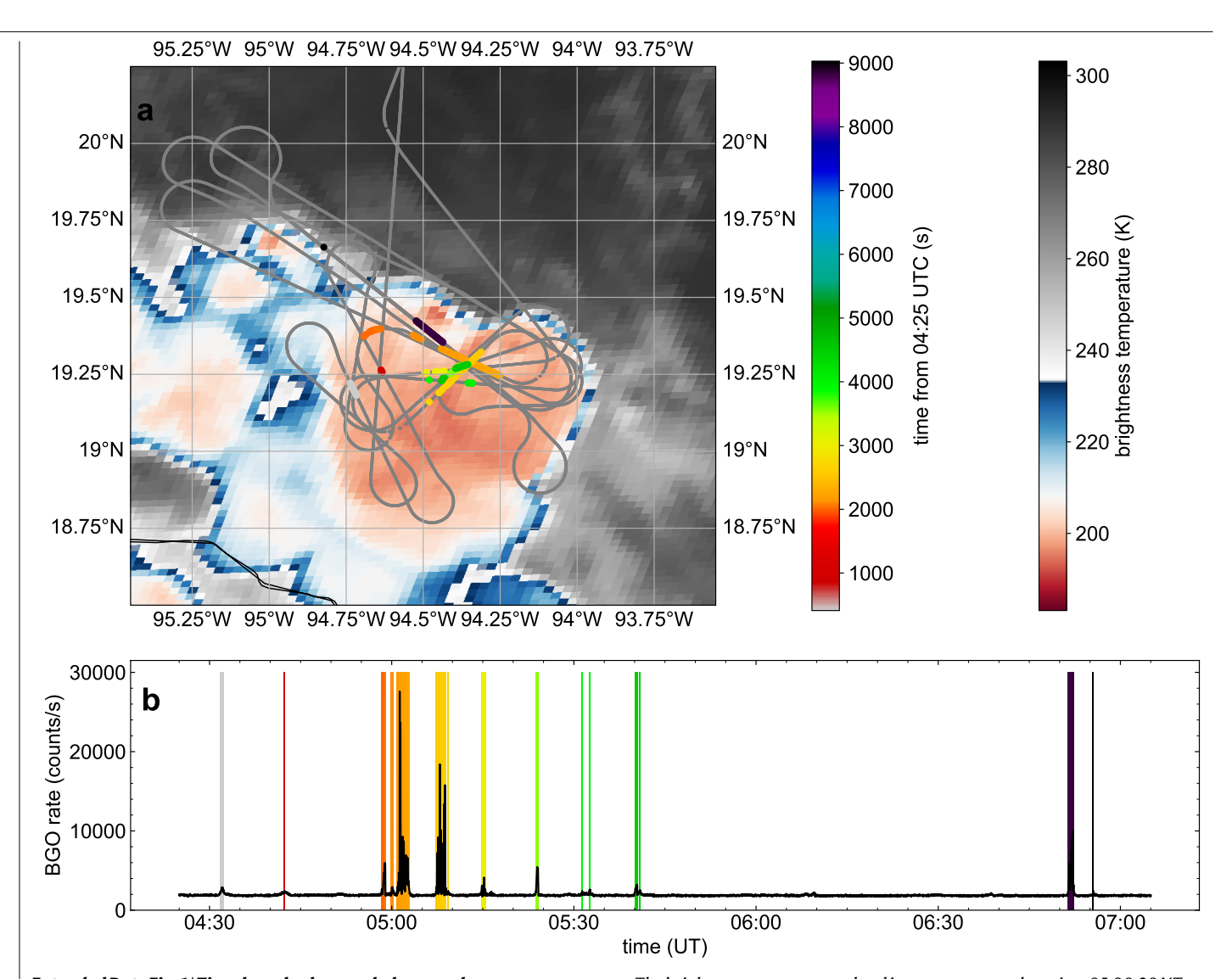
Competing interests The authors declare no competing interests.

Additional information

Correspondence and requests for materials should be addressed to M. Marisaldi, N. Østgaard or A. Mezentsev.

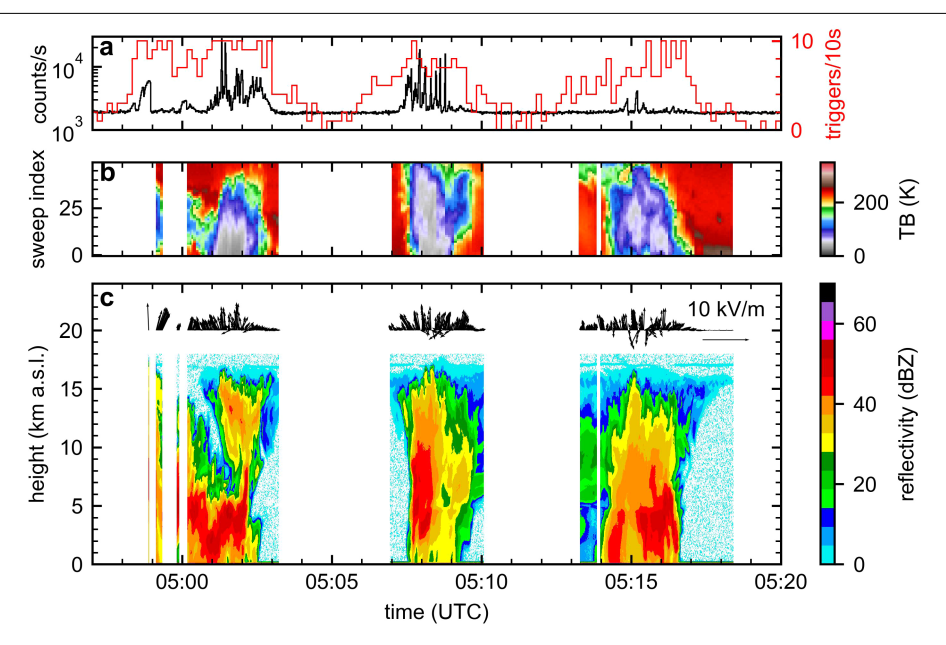
Peer review information *Nature* thanks Joseph Dwyer and Yuuki Wada for their contribution to the peer review of this work.

Reprints and permissions information is available at http://www.nature.com/reprints.



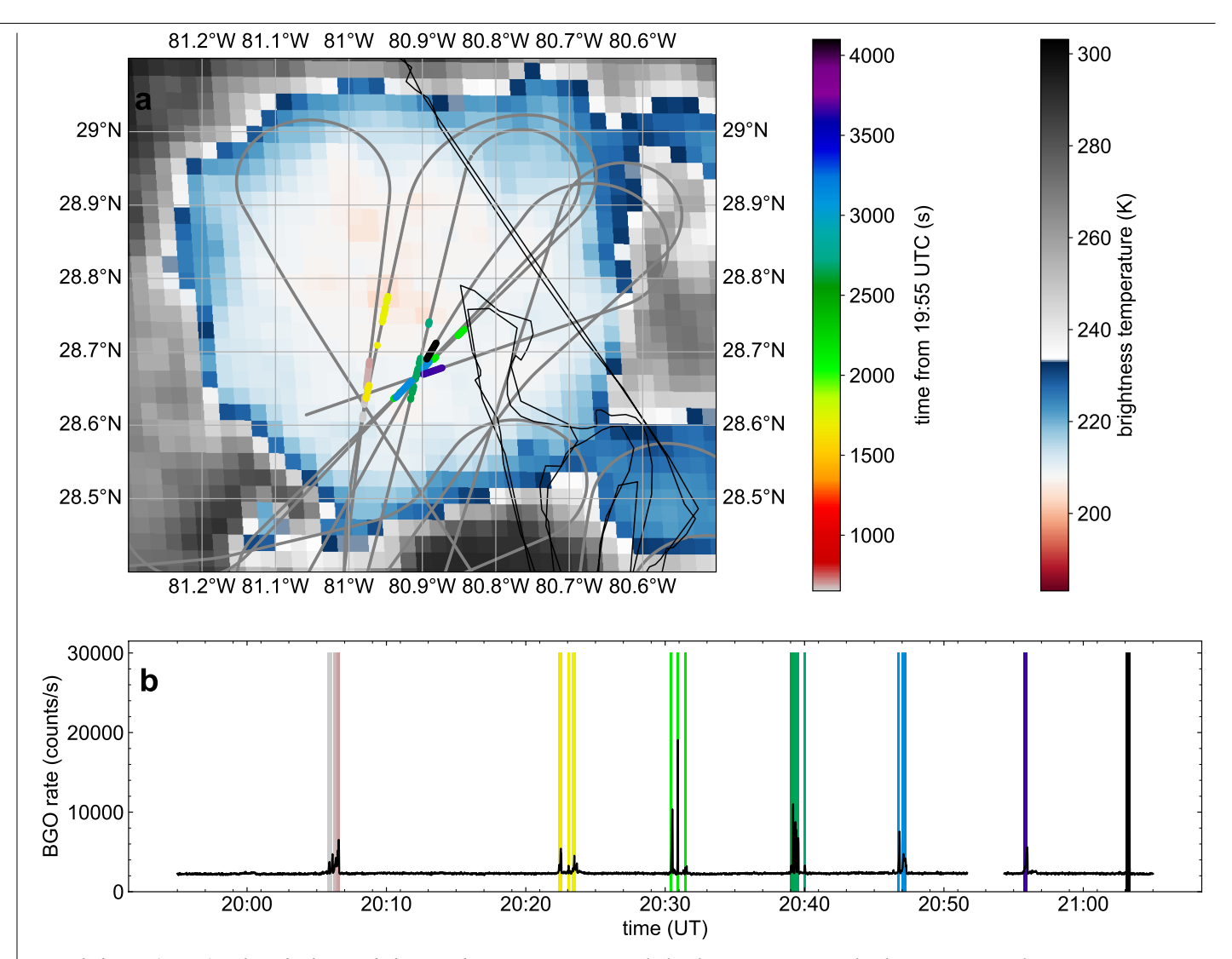
Extended Data Fig. 1 | Time-based colour-coded map and gamma-ray sequence for the flight on 6 July 2023 (Campeche Bay), 04:25-07:05 UT. a, Flight trajectory (grey) overlaid on GOES-18 infrared temperatures, along with marked gamma-ray fluxes exceeding 25% above the background level.

The brightness temperature cloud image corresponds to time 05:00:30 UT. **b**, BGO count rate. Gamma-ray fluxes exceeding 25% above the background level are colour-coded on the basis of time from 04:25:00 UT, correspondingly in panels **a** and **b**.



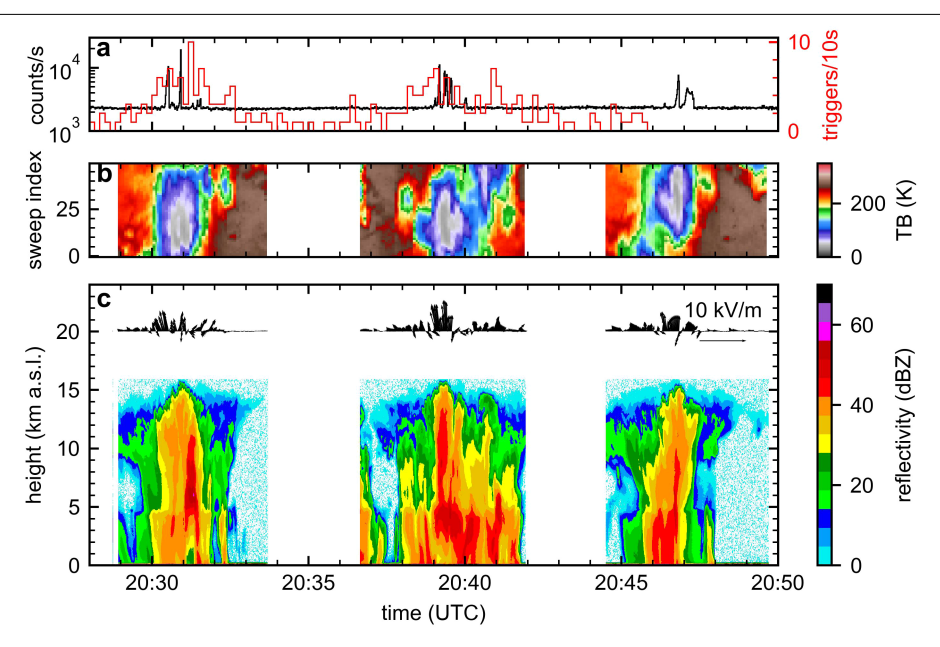
 $\label{lem:extended_DataFig.2} Extended Data Fig. 2 | Gamma-ray count rate with simultaneous electric-field and cloud-characterization data for the flight on 6 July 2023, 04:57–05:20 UT. a, BGO count rate (black, left vertical axis) and EFCM trigger rate (red, right vertical axis). b, Brightness temperature (TB) from AMPR 85.5 GHz Channel A. Sweep index 0 (49) corresponds to scan direction 45° from nadir$

towards starboard (port). **c**, Vertical radar reflectivity profile from EXRAD. Black vectors are the E_{xz} component of the electric field from LIP, in which the x axis is the direction of motion and the z axis is the upward-pointing vertical direction. AMPR, EXRAD and LIP data are not shown if the roll angle is larger than 2° (aircraft manoeuvring).



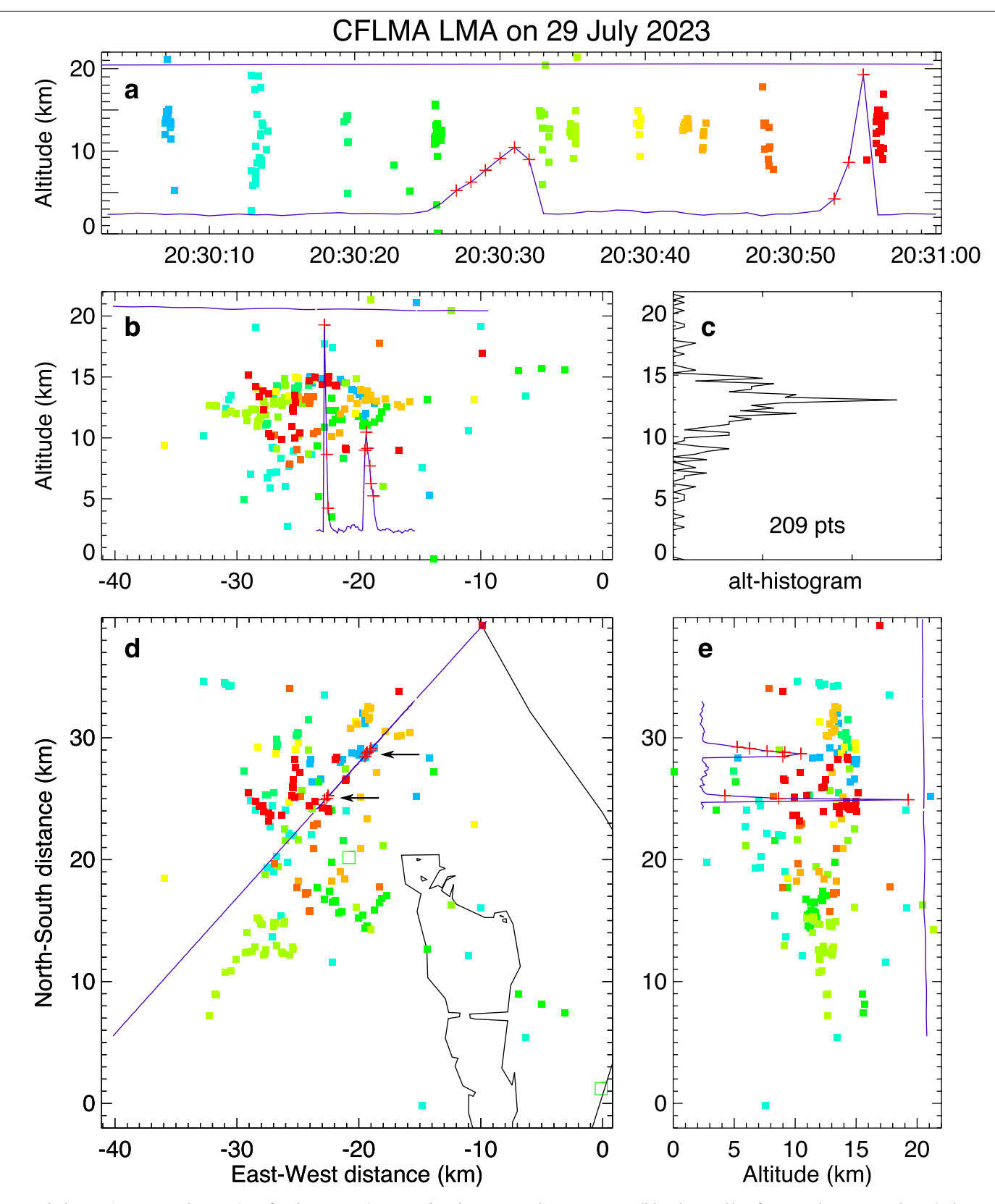
 $\label{lem:extended} \textbf{Extended Data Fig. 3} | \textbf{Time-based colour-coded map and gamma-ray sequence for the flight on 29 July 2023 (Florida, east coast), 19:55–21:05 UT. a, Flight trajectory (grey) overlaid on GOES-16 infrared temperatures, along with marked gamma-ray fluxes exceeding 25% above the background level.}$

The brightness temperature cloud image corresponds to time 20:31:17 UT. **b**, BGO count rate. Gamma-ray fluxes exceeding 25% above the background level are colour-coded on the basis of time from 19:55:00 UT, correspondingly in panels **a** and **b**.



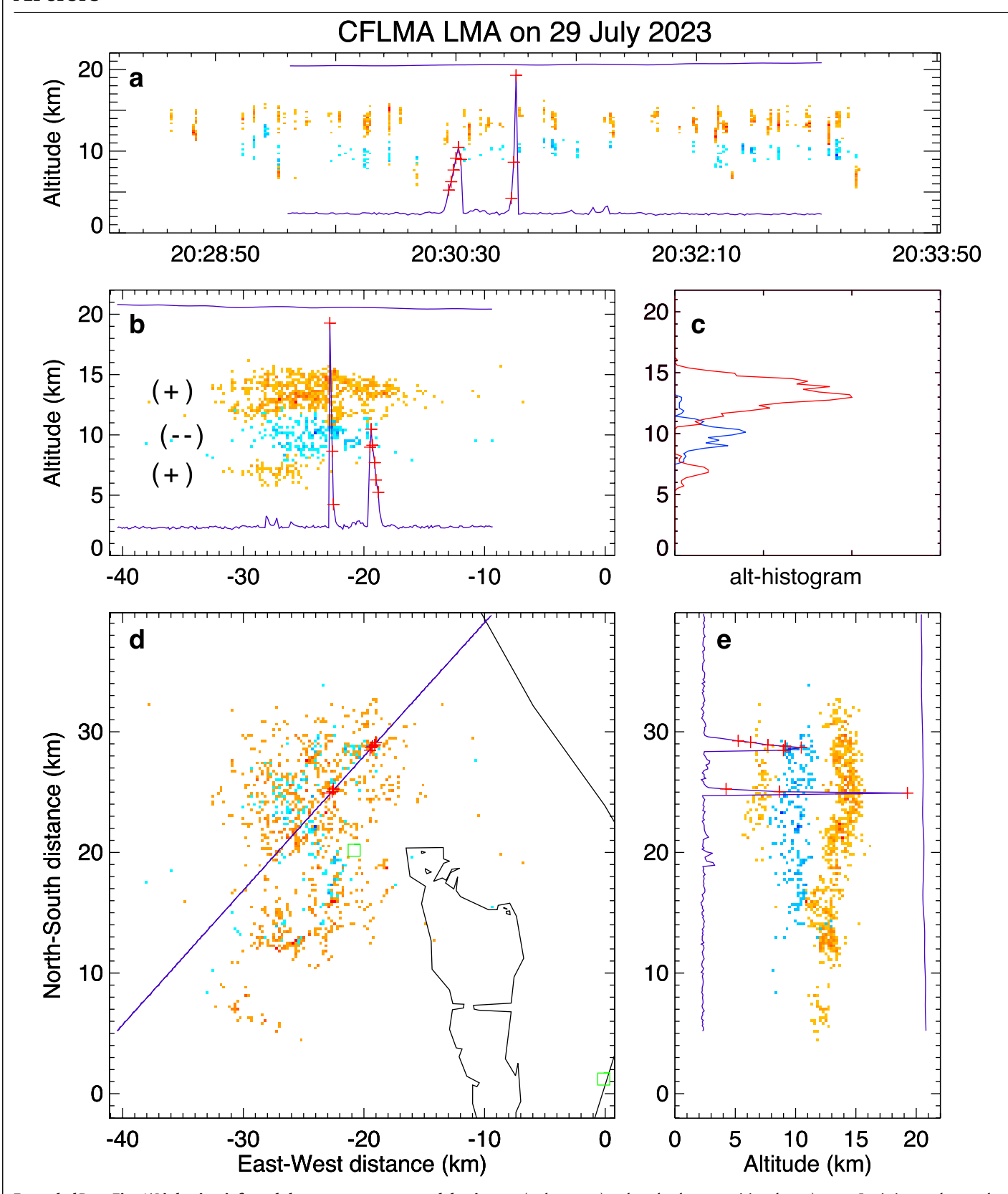
Extended Data Fig. 4 | Gamma-ray count rate with simultaneous electric field and cloud characterization data for the flight on 29 July 2023, 20:28–20:50 UT. a, BGO count rate (black, left vertical axis) and EFCM trigger rate (red, right vertical axis). EFCM data were lost between 20:45:44 and 20:56:00 as a result of a system failure. b, Brightness temperature (TB) from AMPR 85.5 GHz Channel A. Sweep index 0 (49) corresponds to scan direction

 45° from nadir towards starboard (port). **c**, Vertical radar reflectivity profile from EXRAD. Black vectors are the E_{xz} component of the electric field from LIP, in which the x axis is the direction of motion and the z axis is the upward-pointing vertical direction. AMPR, EXRAD and LIP data are not shown if the roll angle is larger than 2° (aircraft manoeuvring).



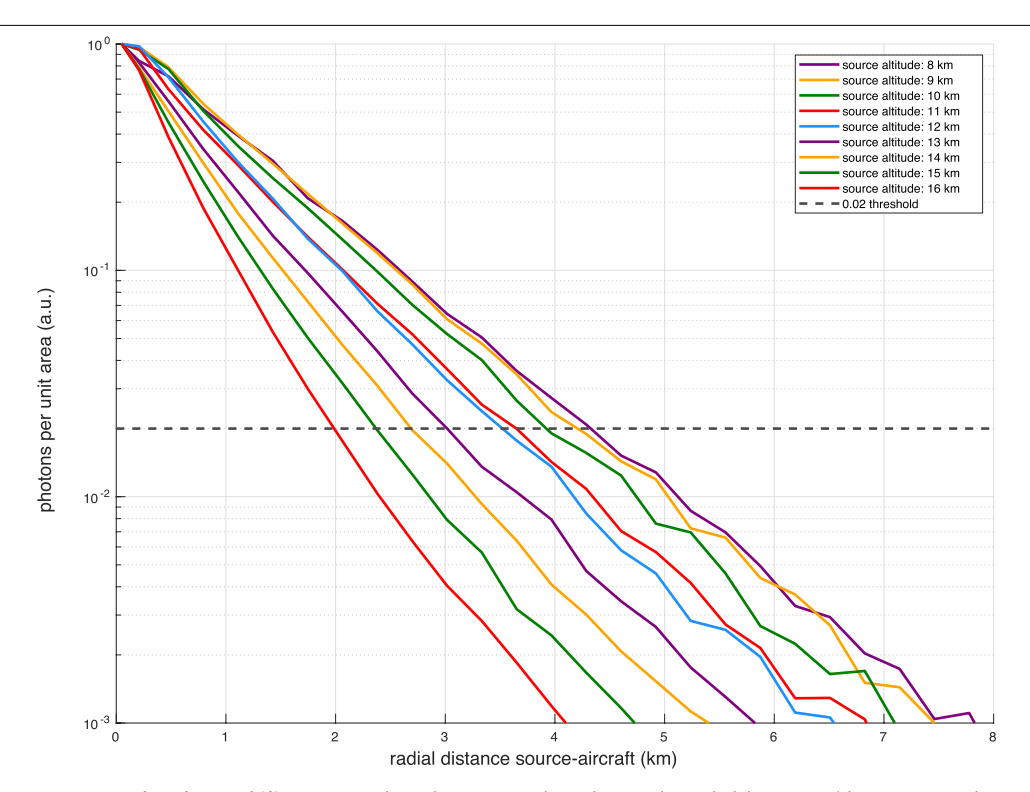
 $\label{lem:extended} \textbf{Data} \ \textbf{Fig.} \ \textbf{5} \ | \ \textbf{LMA} \ \textbf{observations} \ \textbf{for} \ \textbf{the} \ \textbf{energetic} \ \textbf{two-pulse} \ \textbf{glow} \ \textbf{event} \ \textbf{at} \ \textbf{20:30} \ \textbf{UT} \ \textbf{on} \ \textbf{29} \ \textbf{July} \ \textbf{2023.a}, \ \textbf{7} \ \textbf{emporal} \ \textbf{comparison} \ \textbf{of} \ \textbf{the} \ \textbf{1-s} \ \textbf{averaged} \ \textbf{BGO} \ \textbf{count} \ \textbf{rate} \ (\textbf{blue} \ \textbf{line} \ \textbf{and} \ \textbf{red} \ \textbf{'+'} \ \textbf{signs}) \ \textbf{with} \ \textbf{the} \ \textbf{occurrence} \ \textbf{of} \ \textbf{lightning} \ \textbf{in} \ \textbf{the} \ \textbf{storm} \ (\textbf{square} \ \textbf{dots}, \ \textbf{coloured} \ \textbf{by} \ \textbf{time}). \ \textbf{b,e}, \ \textbf{East-west} \ \textbf{and} \ \textbf{north-south} \ \textbf{vertical} \ \textbf{projections} \ \textbf{of} \ \textbf{the} \ \textbf{LMA} \ \textbf{sources} \ \textbf{and} \ \textbf{the} \ \textbf{spatial} \ \textbf{extent} \ \textbf{of} \ \textbf{the} \ \textbf{glows} \ \textbf{and} \ \textbf{the} \ \textbf{height} \ \textbf{of} \ \textbf{the} \ \textbf{ER-2} \ \textbf{relative} \ \textbf{to} \ \textbf{the} \ \textbf{lightning}. \ \textbf{d}, \ \textbf{Plan} \ \textbf{view} \ \textbf{of} \ \textbf{the} \ \textbf{LMA} \ \textbf{sources} \ \textbf{sources} \ \textbf{of} \ \textbf{the} \ \textbf{LMA} \ \textbf{outh} \ \textbf$

and ER-2 trajectory (blue diagonal line from northeast to southwest), showing the location of the ER-2 at the time of the glows (horizontal arrows) relative to the LMA sources (black lines show coastal and inland water boundaries around Kennedy Space Center, green squares show locations of two LMA stations). \mathbf{c} , Histogram of the source altitudes.



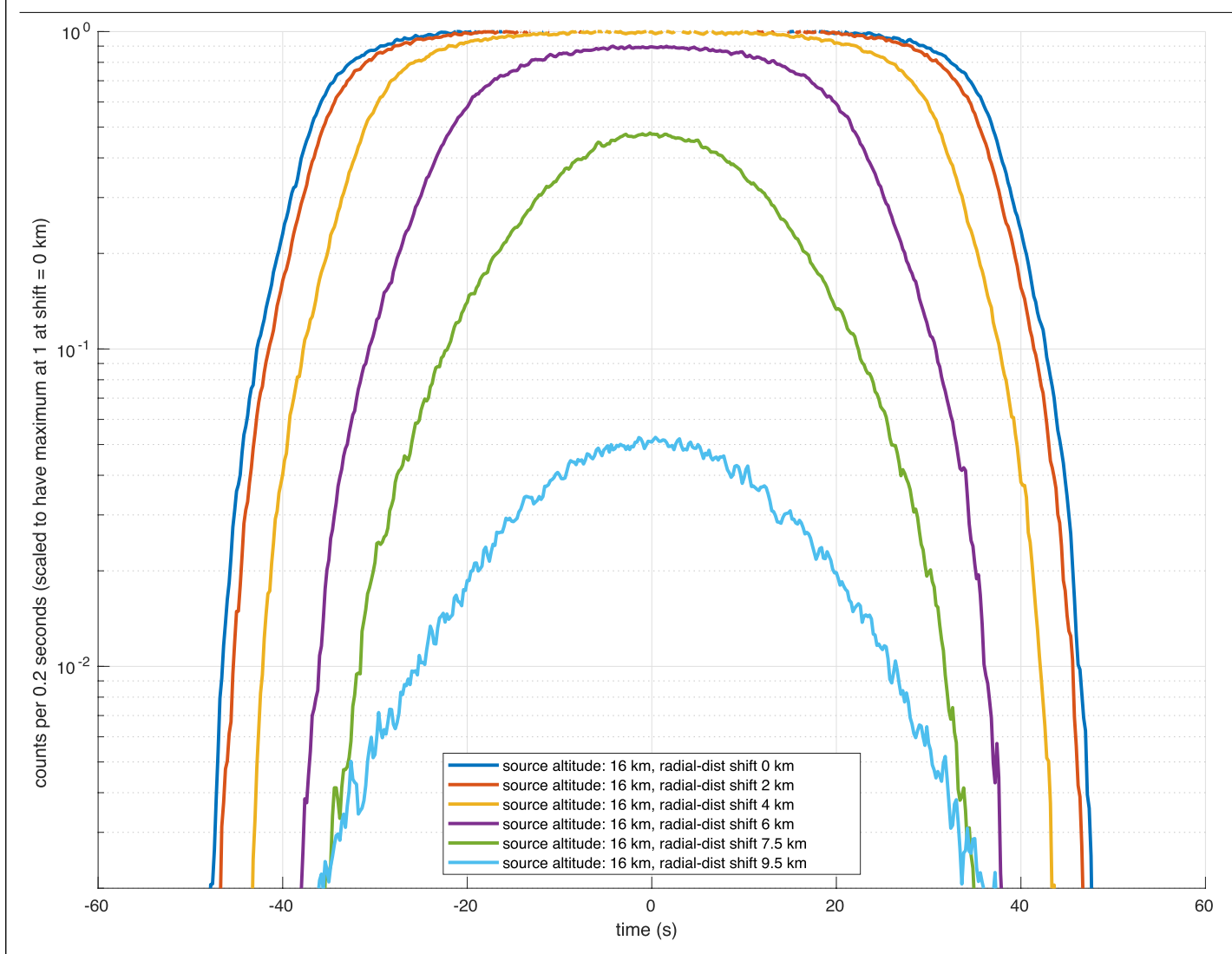
Extended Data Fig. 6 | Lightning-inferred charge structure around the time of the 20:30 glows. Same as Extended Data Fig. 5, except showing the typical tripolar structure (main mid-level negative (blue) and upper positive charges

 $(red-orange)\ and\ weaker lower positive\ charge)\ over\ a\ 5-min\ interval\ around\ the\ time\ of\ the\ glow\ sequence.$

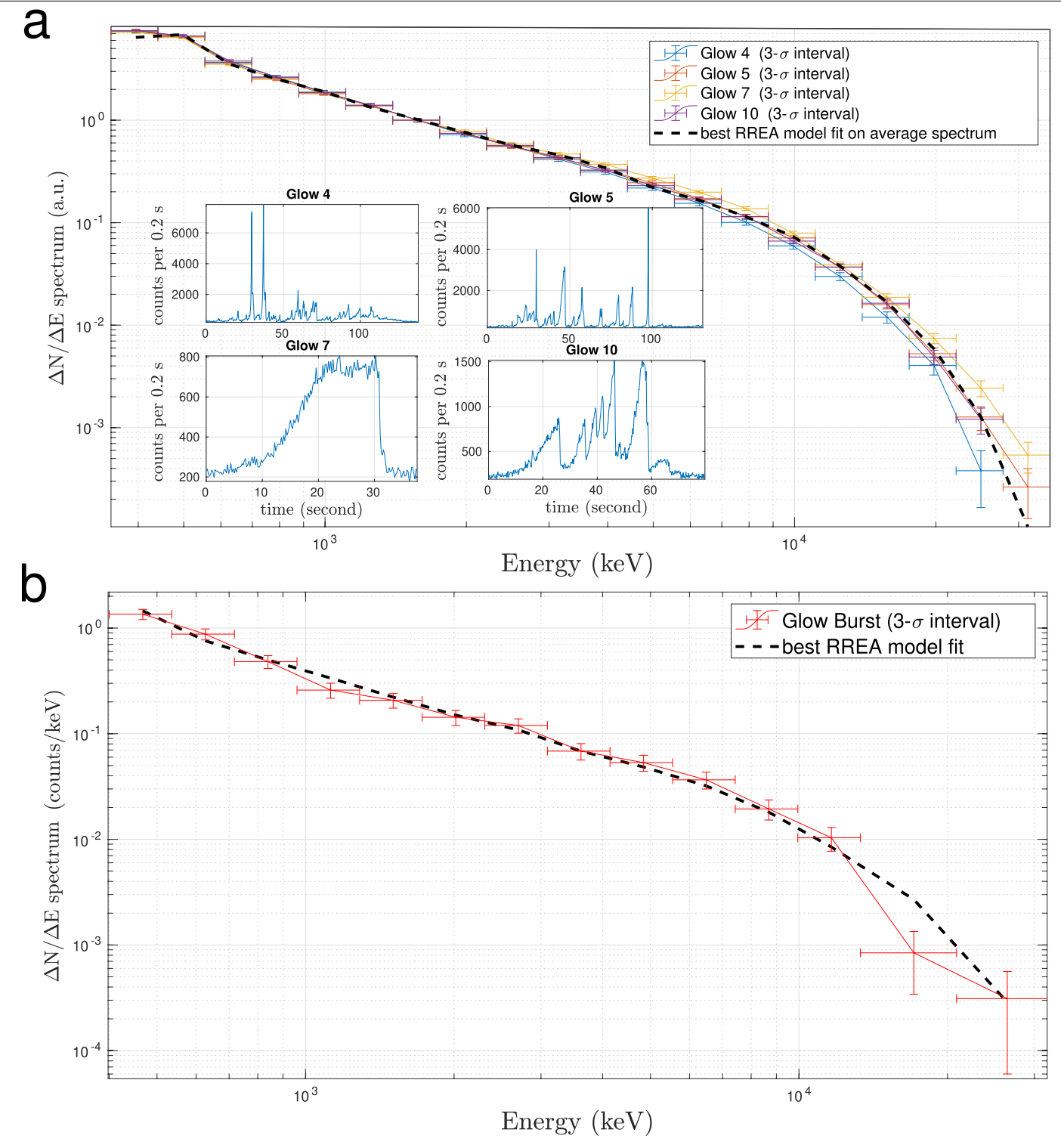


 $\label{lem:extended} \textbf{Extended Data Fig. 7} | \textbf{Gamma-ray-glow detectability.} \ \texttt{Expected number} \\ of photons per unit area at 20-km altitude (arbitrary units, normalized to 1 at radial distance 0) for sources at different altitudes and radial distance from the aircraft. Assuming a maximum intensity of about 12 times the background for the part of the part o$

glows detected at radial distance 0 (the maximum observed intensity), the dashed horizontal line marks the detection threshold for gamma-ray glows 25% above the background.



 $\textbf{Extended Data Fig. 8} \ | \ \textbf{Count-rate variability owing to aircraft motion.} \ \text{Relative number of counts at aircraft altitude assuming the aircraft flying towards an extended source (7.5-km-radius disk) at 16-km altitude for different radial offsets.}$



Extended Data Fig. 9 | Gamma-ray glow and glow-burst spectra.

 $\label{eq:abs} {\bf a}, Background-subtracted differential energy spectra for four time intervals including several glows detected on 6 July 2023. Error bars are three standard deviations. The insets show the BGO count rates. The corresponding time intervals (start time–stop time, UT) are: glow 4, 05:00:49–05:03:07; glow 5,$

 $05:07:09-05:09:20; glow 7, 05:23:35-05:24:13; glow 10, 06:51:13-06:52:33. \\ \textbf{b}, Background-subtracted differential energy spectra for the glow burst detected on 24 July 2024 at 06:44:59.182 UT. Error bars are three standard deviations.$

Extended Data Table 1 | ALOFT flights summary table

Flight n.	Flight date, time	Duration (hours)	Region	N. of glow episodes	N. of glows
1	3-4 July 2023, 2100-0300 UT	6	Yucatan	3	15
2	6 July 2023, 0200-1000 UT	8	Campeche Bay	14	87
3	8 July 2023, 0200-1000 UT	8	El Salvador	5	17
4	12-13 July 2023, 2300-0200 UT	3	Florida	0	0
5	16 July 2023, 1200-1900 UT	7	San Andrés	4	10
6	20-21 July 2023, 2100-0100 UT	4	Florida	4	10
7	24 July 2023, 0300-1100 UT	8	Campeche Bay	34	392
8	25-26 July 2023, 2300-0700 UT	8	Inland Mexico	7	37
9	28 July 2023, 1300-2100 UT	8	San Andrés	1	2
10	29 July 2023, 1800-2300 UT	5	Florida	10	38

Overview of the flight campaign including flight dates, durations, target locations and total number of observed glow episodes and gamma-ray glows.